Modeling and Performance Assessment of the Split-Pi Used as a Storage Converter in All the Possible DC Microgrid Scenarios. Part I: Theoretical Analysis

Massimiliano Luna [1] , **Antonino Sferlazza** [2,*], **Angelo Accetta** [1] , **Maria Carmela Di Piazza** [1] , **Giuseppe La Tona** [1] and **Marcello Pucci** [1]

1 Istituto di Ingegneria del Mare (INM), Consiglio Nazionale delle Ricerche (CNR), Via Ugo La Malfa 153, 90146 Palermo, Italy; massimiliano.luna@cnr.it (M.L.); angelo.accetta@cnr.it (A.A.); mariacarmela.dipiazza@cnr.it (M.C.D.P.); giuseppe.latona@cnr.it (G.L.T.); marcello.pucci@cnr.it (M.P.)
2 Dipartimento di Ingegneria (DI), Università degli Studi di Palermo, Viale delle Scienze ed.10, 90128 Palermo, Italy
* Correspondence: antonino.sferlazza@unipa.it

Abstract: The integration of an electrical storage system (ESS) into a DC microgrid using a bidirectional DC/DC converter provides substantial benefits but requires careful design. Among such converter topologies, the Split-pi converter presents several merits at the cost of non-isolated operation. However, the few works in the literature on the Split-pi presented only closed-loop control with a single control loop; furthermore, they neglected the reactive components' parasitic resistances and did not perform any experimental validation. This work aimed at investigating the use of the Split-pi converter as a power interface between an ESS and a DC microgrid. Five typical microgrid scenarios are presented, where each of which requires a specific state-space model and a suitable control scheme for the converter to obtain high performance. In this study, two different state-space models of the converter that consider the parasitic elements are presented, the control schemes are discussed, and criteria for designing the controllers are also given. Several simulations, as well as experimental tests on a prototype realized in the lab, were performed to validate the study. Both the simulation and experimental results will be presented in part II of this work. The proposed approach has general validity and can also be followed when other bidirectional DC/DC converter topologies are employed to interface an ESS with a DC microgrid.

Keywords: Split-pi; bidirectional converter; electrical storage system; DC microgrid; droop control; current control; feed-forward control

1. Introduction

Over the last few years, DC distribution in terrestrial and marine power systems has attracted a growing interest in view of the implementation of the smart microgrid paradigm due to its advantages in terms of simpler and more efficient electrical architectures. Consequently, power electronic converters that interface distributed generation units, loads, and above all, electrical storage systems (ESSs) with a common DC bus are the subject of renewed interest [1–3]. ESSs have manifold beneficial impacts on DC microgrids: they allow for improving stability and resiliency, compensate for the intermittency of renewable generation, provide ramping support to generators, and act as backup power sources. Furthermore, ESSs ensure a power buffer that can be leveraged to apply suitable energy management strategies to microgrids. In particular, energy management systems (EMSs) can be used to compute the optimal values of power flows among the microgrid devices, which allow for pursuing chosen objectives, such as a minimum electricity bill, maximum efficiency, minimum fuel consumption, or minimum greenhouse gas emissions [1,4–6].

Depending on the designer's choice, the microgrid voltage can be controlled either stiffly using a single voltage generator or in a droop scheme using one or more voltage

generators with a predefined power-sharing ratio, usually in proportion to their power rating (grid-forming generators). When an EMS is used, the other active devices of the microgrid must be controlled as current generators based on the optimal power flows that are computed by the EMS [1,5]. Therefore, depending on the specific configuration, the converter interfacing the ESS with the microgrid must be operated as a stiff voltage generator, a non-stiff voltage generator, or a current generator.

The scientific literature provides several contributions on bidirectional DC/DC converters (BDCs). Reference [7] presented an overview of BDCs, where, besides the review of both non-isolated and isolated configurations, the most relevant control schemes and switching strategies were analyzed. In some applications, galvanic isolation between the input and output side of the converter is required; in such cases, the most frequent choice is the dual active bridge converter (DAB) due to its many advantages [7–9]. However, isolation is mandatory only when very high voltage gain is needed. Non-isolated converters are thus more attractive when the goal is to improve the efficiency, size, weight, and cost of the system [7,10]. A review of non-isolated BDCs topologies was presented in [10]. The advantages and disadvantages of the considered converters were properly highlighted. For example, some converters provide an output voltage with opposite polarity than the input, some draw discontinuous current from the battery, while others require a tapped inductor or exhibit weak regulation capability or a high switch count. Overall, Tytelmaier et al. identified the half-bridge converter (HBC) and the related interleaving variants with coupled inductors as the most promising solutions from the efficiency and robustness standpoints [10]. Furthermore, Odo compared three non-isolated BDC topologies with the classical HBC in terms of their suitability for energy storage in a DC microgrid and identified the cascaded buck-boost HBC topology as the best compromise [11].

An interesting alternative is offered by the Split-pi converter, which is a non-isolated BDC that is based on two cascaded HBCs with a common bulk capacitor instead of a common inductor. As such, it is the dual topology of the cascaded buck-boost HBC that was analyzed in [7,10,11]. The Split-pi was initially developed for electric vehicles and patented in 2004 [12], and it is receiving increasing attention due to its distinct advantages [13–20]. It exhibits high efficiency, like the DAB, but with a reduced switch count (eight vs. four switches, of which, only two are actively commutated). Furthermore, LC filters at both ports of the Split-pi allow for small reactive components and reduce the switching noise. On the other hand, the additional phase delay introduced by such filters can slightly complicate this converter's control with respect to simpler converters [17,18]. Nonetheless, the control of the Split-pi is less complicated than that of the DAB because it requires conventional duty cycle control of the pulse width modulator (PWM) instead of phase shift control. An additional advantage of the Split-pi is its suitability for multiphase systems, where a significant reduction in component size and cost can be attained. These features make it attractive when high power density is required, such as in hybrid electric vehicles, renewable energy systems, and aerospace/marine/military applications [16,17].

Only three papers in the technical literature proposed applications in which the Split-pi converter was not controlled using an open-loop [16,17,19]. The aim of [17] was to study a system in which the Split-pi interfaced a flywheel with a 12 V, 120 W DC bus connecting a photovoltaic generator with a passive load. However, in the related control scheme, only one control loop was active at a time (either for the output voltage or the input current) using a shared controller, and the choice was made using a rule-based approach. Singhai et al. did not focus on a specific application and presented a state-space model of the Split-pi converter and a transfer function to design a closed-loop controller for its output voltage [16]. However, they considered the converter connected to a passive load and neglected the parasitic resistances. Finally, Monteiro et al. considered a Split-pi converter with a multilevel structure and controlled current or voltage in any of the two ports in an open-loop, whereas the common DC-link voltage was controlled in a closed-loop [19]. Only a few details about the control systems were given because the study mainly focused on comparing the multilevel Split-pi topology and the interleaved topology of [20].

Apart from [17], all these works only presented simulation results without experimental validation. Furthermore, they all studied closed-loop control with a single control loop, neglecting the reactive components' parasitic resistances. However, when the converter is used to interface an ESS with an active load, such as a DC microgrid, it is essential to control both the ESS current and the output voltage/current of the converter, as required by the microgrid designer. Furthermore, the parasitic elements cannot be neglected because they affect the losses and the maximum gain attainable using the converter.

To cover these aspects, in this work, the use of the Split-pi converter in such an application was investigated with particular attention to its model, the design of its control system, and the assessment of the expected performance in all the possible microgrid configurations. In this first part of the work, it was shown that the Split-pi must be modeled in two different ways depending on the microgrid scenario and that control schemes involving a different number of control loops are needed. In the case of the output voltage control, a feed-forward action was also required to obtain high performance. Furthermore, it was shown that conventional PI regulators alone were not sufficient to obtain the desired performance for output current control in stiff microgrids. The two state-space models considering the parasitic elements and the transfer functions of interest were given in the study, together with criteria to design the controllers. The chosen case study was a DC microgrid that was representative of both terrestrial and marine applications. In Part II of the work, a comprehensive performance assessment is presented based on simulations and experimental tests that validate the study. Finally, the proposed approach has general validity and can also be followed when other BDC topologies are used to interface a storage system with a DC microgrid.

2. Topology, Operation Modes, and Sizing of the Split-Pi Converter

The schematic of a symmetrical Split-pi converter is sketched in Figure 1, including its reactive components' parasitic resistances. Such a converter can be viewed as the cascaded connection of a first HBC at port 1, a bulk capacitor, and another HBC at port 2. Since the two HBCs are bidirectional, the whole Split-pi converter is also a BDC. If the two HBCs have equal reactive components, the Split-pi is said to be symmetrical.
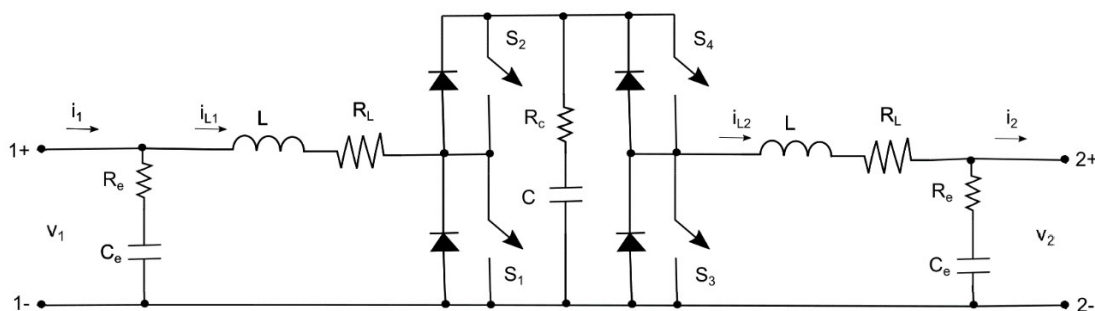
Figure 1. Schematic of the symmetrical Split-pi converter.

The four switches (S1–S4) were sketched in Figure 1 as ideal switches. In the original formulation of [12], they were implemented using MOSFETs to exploit the advantage of synchronous rectification. According to [12], the Split-pi has four operation modes, depending on the relationship between V_1 and V_2 and on the power direction, as summarized in the first four rows of Table 1, which is an extension of the table reported in [18]. In this work, the Split-pi converter was used to interface a storage system (connected to port 1) with a DC microgrid (connected to port 2). It is worth noting that, whenever possible, the storage system is chosen so that $V_1 \leq V_2$ for both technical and safety reasons. Hence, the present work considered the Split-pi converter operating in modes 1 and 2.

Table 1. Summary of the operating modes of the Split-pi converter.

Mode	$V_1 \leq V_2$	Power Direction	Split-Pi Operation	Duty Cycle of S1	Duty Cycle of S2	Duty Cycle of S3	Duty Cycle of S4	Gain of the Split-Pi in Direction $1 \rightarrow 2$
1	Yes	$1 \rightarrow 2$	Boost for $1 \rightarrow 2$	d	$1-d$	0	1	$\frac{1}{1-d}$
2	Yes	$2 \rightarrow 1$	Buck for $2 \rightarrow 1$	d	$1-d$	0	1	$\frac{1}{1-d}$
3	No	$1 \rightarrow 2$	Buck for $1 \rightarrow 2$	0	1	$1-d$	d	d
4	No	$2 \rightarrow 1$	Boost for $2 \rightarrow 1$	0	1	$1-d$	d	d

The Split-pi components can be sized according to the classical formulas used for buck and boost converters [17,21]. Specifically, the minimum inductance value is expressed by (1) for both boost and buck operations; on the other hand, the minimum capacitance of the input and output capacitors C_e can be computed using (2), which is valid for a buck converter, whereas the minimum value of the bulk capacitance C is expressed by (3), which is valid for a boost converter:

$$L_{min} = \frac{100 \, V_2(1-d)d}{2F_{sw}r_{i\%}I_1}, \tag{1}$$

$$C_{e, \, min} = \frac{100(1-d)}{8F_{sw}^2 r_{ve\%}L}, \tag{2}$$

$$C_{min} = \frac{100 \, I_2 d}{F_{sw}r_{v\%}V_2}. \tag{3}$$

In (1), (2), and (3), F_{sw} is the switching frequency; d is the duty cycle; V_2 and I_2 are the output voltage and current, respectively; I_1 is the input current; $r_{i\%}$ is the desired inductor current ripple; and $r_{v\%}$ and $r_{ve\%}$ are the desired voltage ripple values on the bulk and external capacitors, respectively.

3. Possible DC Microgrid Scenarios, Load Models, and Required Control Schemes for the ESS Converter

In the present study, it was supposed that the Split-pi converter was used to interface an ESS with a DC microgrid. Under this hypothesis, several scenarios could be considered depending on the control mode chosen for both the storage-side converter and the grid-side converters interfacing other microgrid generators, if any. Depending on the combinations of the control modes of such converters, five scenarios were identified and, for each of them, a different type of load model and control scheme must be used. The different DC microgrid scenarios and the required load models and control schemes are discussed in the following subsections.

3.1. Possible DC Microgrid Scenarios

In general terms, one of the following situations can occur as a control mode for the microgrid converters:

- All the generator converters are controlled in droop mode to regulate the microgrid voltage with a predefined power-sharing ratio. Thus, each generator behaves as an ideal voltage generator with a series-connected resistance. The droop scheme leads to a simple but very reliable microgrid and does not require a communication infrastructure. If a storage system is present, its droop characteristic is usually chosen so that no current is supplied at half the rated load of the microgrid, whereas charging/discharging occurs for load power below/above such a value. If there is only one active device in the microgrid (either a storage system or a generator), it could also be controlled with a null droop resistance (stiff microgrid) so that the microgrid voltage does not vary with load power
- The microgrid follows a master–slave architecture: some converters for generators or storage systems (i.e., the masters) are controlled in droop mode (a null droop resistance

is possible only with a single master); the others (i.e., the slaves) behave as current generators and are managed by an EMS to pursue one or more predefined goals.

Therefore, three control modes are possible for both the storage-side and grid-side converters: stiff droop control, non-stiff droop control, and current control. The five scenarios resulting from the combinations of the control modes of such converters are described in the first three columns of Table 2. For the sake of clarity, such scenarios are referred to also by means of an abbreviation in the form Sx-Gy, where x and y specify the control mode for the storage-side and the grid-side converters, respectively. The range of options for x is:

- C for current control.
- D for non-stiff droop control.
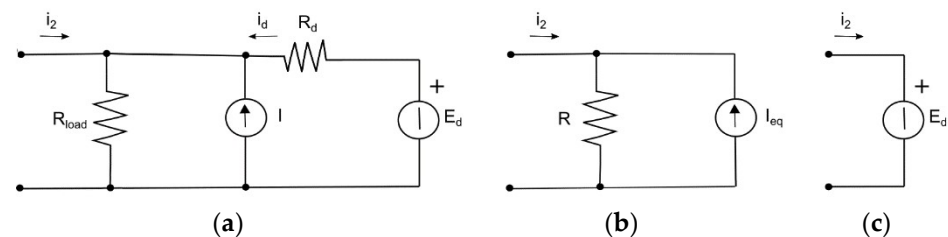- S for stiff droop control.

Figure 2. Equivalent active load transformations for non-stiff and stiff microgrids: (**a**) general load model for storage converter; (**b**) equivalent load model considered in scenarios #1–#4; (**c**) equivalent load model considered in scenario #5.

Table 2. Possible combinations of microgrid scenarios, converter and load models, and control schemes for the Split-pi.

Microgrid Scenario	Storage Converter	Other Generators	State-Space Model of the Split-Pi	Load for the State-Space Model of the Split-Pi	Control Scheme
#1 (SS-GN)	Droop mode with $R_d = 0$ (stiff microgrid)	No other generator present (passive load) or all current controlled by the EMS	Model A	R and I_{eq}, as in Figure 2b	2 loops + FF, as in Figure 3 with $R_{ds} = 0$
#2 (SD-GN)	Droop mode with $R_d \neq 0$	No other generator present (passive load) or all current controlled by the EMS	Model A	R and I_{eq}, as in Figure 2b	3 loops + FF, as in Figure 3
#3 (SD-GD)	Droop mode with $R_d \neq 0$	At least one is droop controlled and none has $R_d = 0$	Model A	R (low) and I_{eq}, as in Figure 2b	3 loops + FF, as in Figure 3
#4 (SC-GD)	Current mode	At least one is droop controlled and none has $R_d = 0$	Model A	R (low) and I_{eq}, as in Figure 2b	2 loops, as in Figure 4
#5 (SC-GS)	Current mode	One is droop controlled and has $R_d = 0$ (stiff microgrid); the others, if present, are current controlled by the EMS	Model B	E_d, as in Figure 2c	2 loops, as in Figure 4

As for the options for y:

- N if no grid-side generator is present or if none of the grid-side generators are operated with droop control.
- D if at least one generator is droop controlled but not in a stiff way.
- S if there is one generator operated with stiff droop control; in such a case, the other grid-side generators, if present, must be current controlled by the EMS.

3.2. Possible Load Models for the ESS Converter

The dynamic behavior of the storage converter is affected by the load that it must supply, which depends not only on the passive loads of the DC microgrid but also on the possible presence of grid-side generators. In the most general case, the load for the ESS

converter can be modeled following these steps: (1) aggregating all the droop-controlled generators of the microgrid using Thevenin's theorem, obtaining parameters E_d and R_d; (2) combining all the current-controlled generators managed by the EMS to compute the overall current I; (3) including an aggregated passive load R_{load}. The resulting circuit model is shown in Figure 2a. However, it is convenient to reduce such a model to a suitable equivalent form comprising only one generator. Toward this aim, it is necessary to distinguish between the five scenarios. In scenarios #3 (SD-GD) and #4 (SC-GD), using Norton's theorem, the couple E_d, R_d can be substituted with an equivalent current generator E_d/R_d and a parallel-connected resistance R_d. Then, the load can be reduced to that of Figure 2b with the following assumptions: $I_{eq} = I + E_d/R_d$ and $R = R_{load}//R_d$, where $//$ denotes the parallel connection of circuit elements. In scenarios #1 (SS-GN) and #2 (SD-GN), the same scheme of Figure 2b can be used assuming $I_{eq} = I$ and $R = R_{load}$. Furthermore, in scenario #5 (SC-GS), the converter's output voltage is set equal to E_d because $R_d = 0$. Since both R_{load} and I are now parallel connected to an ideal voltage generator, they do not influence the converter's dynamics. Thus, the load can be modeled as shown in Figure 2c.
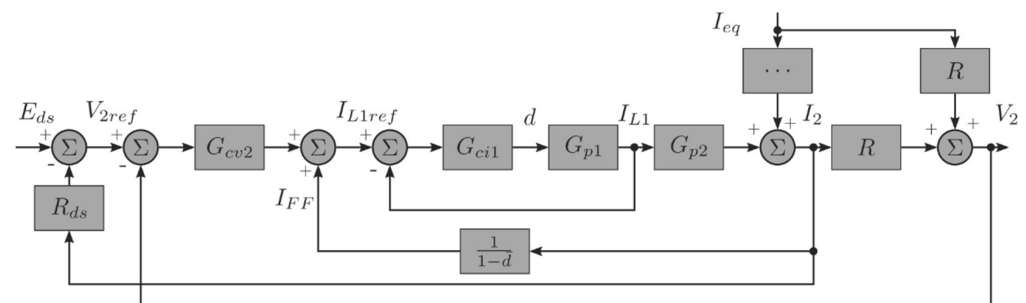

Figure 3. Control scheme that is used for the voltage control of the ESS converter in scenarios #1 (SS-GN), #2 (SD-GN), and #3 (SD-GD).
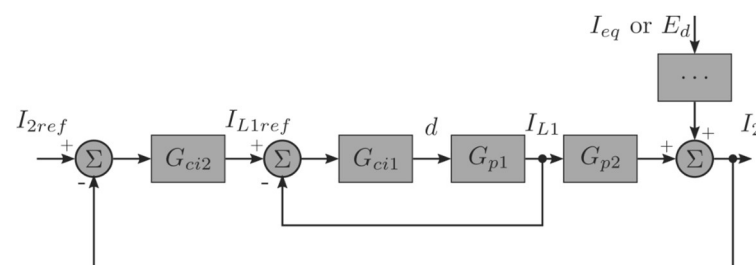

Figure 4. Control scheme that is used for the current control of the ESS converter in scenarios #4 (SC-GD) and #5 (SC-GS).

In the following, the state-space model of the storage converter connected to the load of Figure 2b is denoted as model A, whereas model B refers to the converter connected to the load of Figure 2c. The derivation of such models is given in Section 4. The relationship between the possible DC microgrid scenarios and the storage converter and load models is described in the first five columns of Table 2. It is worth noting that the value of the equivalent load resistance R considered in scenarios #3 (SD-GD) and #4 (SC-GD) is much lower than that of scenarios #1 (SS-GN) and #2 (SD-GN) because it results from the parallel connection of R_{load} and R_d. Finally, the last column of Table 2 reports the required control scheme for the ESS converter in each microgrid scenario according to the considerations given in the following section.

3.3. Required Control Schemes for the ESS Converter

In general, the closed-loop control scheme for the storage converter depends on the microgrid scenario. However, regardless of the scenario, an important goal is to control the current I_{L1} of the leftmost inductor to ensure that it is compatible with the storage system's

current state. Thus, in the related control loop, its reference value should be dynamically saturated to avoid overcharging or overdischarging the storage system.

In the first three scenarios, i.e., SS-GN, SD-GN, and SD-GD, besides the current loop for I_{L1}, a voltage loop is needed to regulate the output voltage V_2 at the nominal voltage V_{2n}. A suitable controller is required in each control loop. Typically, PI or PID regulators with an anti-windup action are used, which must be designed to obtain a stable system with the desired dynamics. In scenarios #2 (SD-GN) and #3 (SD-GD), a third loop is also required to implement the droop characteristic of the storage converter by computing the voltage reference V_{2ref} based on the output current I_2 according to the equation $V_{2,ref} = E_{ds} - R_{ds} \cdot I_2$, where E_{ds} and R_{ds} are the parameters of the droop characteristic of such a converter. The control scheme used in scenarios #1 (SS-GN), #2 (SD-GN), and #3 (SD-GD) is depicted in Figure 3. In particular, the external loop is opened in scenario #1 (SS-GN) because $R_d = 0$. The presence of the current generator I_{eq} in parallel to the load resistance is considered a disturbance that affects the system's output, which will be suitably compensated for by the control system, regardless of the related transfer function. As will be shown in Section 6, when the output voltage V_2 is controlled, a feed-forward (FF) action is also required in addition to the voltage loop to suitably reduce the overshoot. Since I_{eq} cannot be measured, the output current I_2 is chosen as the FF action input.

On the other hand, the converter is current-controlled in scenarios #4 (SC-GD) and #5 (SC-GS). In these cases, besides the inner loop for I_{L1}, another current loop is needed to regulate the output current I_2 based on a reference I_{2ref} that is computed by the EMS. The related control scheme is shown in Figure 4. Again, the external voltage or current generator is considered a disturbance, and the related transfer function is irrelevant.

The type of control scheme to be used in each microgrid scenario and the required number of control loops are reported in the last column of Table 2. It is worth noting that suitable saturators are required in the controllers of each loop (G_{ci1}, G_{cv2}, G_{ci2}). Specifically, the output of the controller G_{ci1} (i.e., the duty cycle d) is bounded by the interval [0; 0.9] to avoid overcurrents due to prolonged transients with $d = 1$. On the other hand, the reference value for I_{L1} (i.e., the output of G_{cv} plus the FF term or the output of G_{ci2}) is bounded by the interval $[-I_{cx}; I_{dx}]$, where I_{cx} and I_{dx} are the maximum charging/discharging currents of the storage system. Finally, the upper or lower bound of such an interval is dynamically replaced with zero if the battery SOC reaches 100% or goes below the minimum allowed SOC, respectively.

4. State-Space Models of the Split-Pi Converter

The two state-space models of a Split-pi converter that interfaces a storage system with a non-stiff (scenarios #1~#4) or stiff (scenario #5) microgrid and operates with $V_1 \leq V_2$ are presented in the following. They consider the parasitic elements and were determined according to the state-space averaging technique [22].

4.1. State-Space Model A: Split-Pi Converter Connected to a Non-Stiff Microgrid

The state-space model of a Split-pi converter connected to a non-stiff microgrid and operating with $V_1 \leq V_2$ can be expressed in matrix form as follows:

$$\begin{cases} \dot{x} = Ax + Bu \\ y = Cx + Du \end{cases} \tag{4}$$

$$x = [I_{L1}, \ I_{L2}, \ V_c, \ V_e]' \tag{5}$$

$$u = [V_1, I_{eq}]' \tag{6}$$

$$y = [I_{L1}, V_2, I_2]' \tag{7}$$

$$\begin{cases} A = dA_{on} + (1-d)A_{off} \\ B = dB_{on} + (1-d)B_{off} \\ C = dA_{on} + (1-d)C_{off} \\ D = dD_{on} + (1-d)D_{off} \end{cases} \tag{8}$$

$$A_{on} = \begin{bmatrix} -\frac{R_L}{L} & 0 & 0 & 0 \\ 0 & -\frac{R_{tot}}{L} & \frac{1}{L} & -\frac{R}{LR_{sum}} \\ 0 & -\frac{1}{C} & 0 & 0 \\ 0 & \frac{R}{R_{sum}C_e} & 0 & -\frac{1}{R_{sum}C_e} \end{bmatrix} \tag{9}$$

$$A_{off} = \begin{bmatrix} -\frac{R_L+R_c}{L} & \frac{R_c}{L} & -\frac{1}{L} & 0 \\ \frac{R_c}{L} & -\frac{R_{tot}}{L} & \frac{1}{L} & -\frac{R}{LR_{sum}} \\ \frac{1}{C} & -\frac{1}{C} & 0 & 0 \\ 0 & \frac{R}{R_{sum}C_e} & 0 & -\frac{1}{R_{sum}C_e} \end{bmatrix} \tag{10}$$

$$B_{on} = B_{off} = \begin{bmatrix} \frac{1}{L} & 0 \\ 0 & -\frac{R_p}{L} \\ 0 & 0 \\ 0 & \frac{R}{R_{sum}C_e} \end{bmatrix} \tag{11}$$

$$C_{on} = C_{off} = \begin{bmatrix} 1 & 0 & 0 & 0 \\ 0 & R_p & 0 & \frac{R}{R_{sum}} \\ 0 & \frac{R_e}{R_{sum}} & 0 & \frac{1}{R_{sum}} \end{bmatrix} \tag{12}$$

$$D_{on} = D_{off} = \begin{bmatrix} 0 & 0 \\ 0 & R_p \\ 0 & -\frac{R}{R_{sum}} \end{bmatrix} \tag{13}$$

where $R_p = R//R_e$, $R_{sum} = R + R_e$, and $R_{tot} = R_p + R_L + R_c$.

Since $B_{on} = B_{off}$ and $D_{on} = D_{off}$, the small-signal behavior of the converter does not depend on the input values. According to the method described in [21], the model can be linearized around a chosen operating point corresponding to the duty cycle $\bar{d}$ and the state $\bar{x} = [I_{L10},\ I_{L20},\ V_{c0},\ V_{e0}]'$, obtaining the following transfer functions:

$$G_{p1}(s) = \frac{\tilde{I}_{L1}}{\tilde{d}} = \frac{n_3 s^3 + n_2 s^2 + n_1 s + n_0}{d_4 s^4 + d_3 s^3 + d_2 s^2 + d_1 s + d_0} \tag{14}$$

$$G_{p2}(s) = \frac{\tilde{I}_2}{\tilde{I}_{L1}} = \frac{R_k I_{L10}}{L^2 CC_e R_{sum}} \cdot \frac{(1 + sR_c C)(1 + sR_e C_e)\left(1 - s\frac{L}{R_k}\right)}{n_3 s^3 + n_2 s^2 + n_1 s + n_0} \tag{15}$$

whose coefficients n_i, d_i, and R_k are given in Appendix A. $G_{p1}(s)$ and $G_{p2}(s)$ are small-signal transfer functions that express the effect of perturbations of a variable on another one (both denoted with a tilde). According to Figure 3, $G_{p1}(s)$ expresses the relationship between d and I_{L1}, whereas $G_{p2}(s)$ describes the dependence of I_2 on I_{L1}. Clearly, the relationship between I_{L1} and V_2 is expressed by $G_{p2}(s) \cdot R$.

4.2. State-Space Model B: Split-Pi Converter Connected to a Stiff Microgrid

In the case of a Split-pi converter operating with $V_1 \leq V_2$ and connected to a stiff microgrid, (4) and (8) are still valid, but (5), (9) and (11) are replaced by (16), (19), and (21), respectively.

$$x = [I_{L1},\ I_{L2},\ V_c,\ V_e]' \tag{16}$$

$$u = [V_1, E_d]' \tag{17}$$

$$y = [I_{L1}, I_2]' \tag{18}$$

$$A_{on} = \begin{bmatrix} -\frac{R_L}{L} & 0 & 0 & 0 \\ 0 & -\frac{R_c+R_L}{L} & \frac{1}{L} & 0 \\ 0 & -\frac{1}{C} & 0 & 0 \\ 0 & 0 & 0 & -\frac{1}{R_e C_e} \end{bmatrix} \tag{19}$$

$$A_{off} = \begin{bmatrix} -\frac{R_c+R_L}{L} & \frac{R_c}{L} & -\frac{1}{L} & 0 \\ \frac{R_c}{L} & -\frac{R_c+R_L}{L} & \frac{1}{L} & 0 \\ \frac{1}{C} & -\frac{1}{C} & 0 & 0 \\ 0 & 0 & 0 & -\frac{1}{R_e C_e} \end{bmatrix} \tag{20}$$

$$B_{on} = B_{off} = \begin{bmatrix} \frac{1}{L} & 0 \\ 0 & -\frac{1}{L} \\ 0 & 0 \\ 0 & \frac{1}{R_e C_e} \end{bmatrix} \tag{21}$$

$$C_{on} = C_{off} = \begin{bmatrix} 1 & 0 & 0 & 0 \\ 0 & 1 & 0 & \frac{1}{R_e} \end{bmatrix} \tag{22}$$

$$D_{on} = D_{off} = \begin{bmatrix} 0 & 0 \\ 0 & -\frac{1}{R_e} \end{bmatrix} \tag{23}$$

Again, the small-signal behavior does not depend on input values. The model can be linearized around a chosen operating point corresponding to $\bar{d}$ and $\bar{x}$, obtaining the transfer functions (24) and (25), whose coefficients n_i, d_i, and R_k are given in Appendix B. According to Figure 4, $G_{p1}(s)$ expresses the relationship between d and I_{L1}, whereas $G_{p2}(s)$ describes the dependence of I_2 on I_{L1}. It is worth noting that a zero-pole cancellation occurs due to the stiff voltage imposed on the $R_e C_e$ branch at port 2; thus, the resulting system's order is three instead of four and the voltage and current on C_e cannot be controlled.

$$G_{p1}(s) = \frac{\widetilde{I}_{L1}}{\widetilde{d}} = \frac{n_2 s^2 + n_1 s + n_0}{d_3 s^3 + d_2 s^2 + d_1 s + d_0} \tag{24}$$

$$G_{p2}(s) = \frac{\widetilde{I}_2}{\widetilde{I}_{L1}} = \frac{R_k I_{L10}}{L^2 C} \cdot \frac{(1+sR_cC)\left(1-s\frac{L}{R_k}\right)}{n_2 s^2 + n_1 s + n_0} \tag{25}$$

5. Case Study and Converter Sizing

In this section, the chosen case study is described and the droop characteristics of both the storage converter and the voltage generator of the microgrid are discussed. Then, the Split-pi converter's reactive components are sized based on the chosen case study's parameters.

With no loss of generality, the proposed investigation was performed by referring to a 48 V, 750 W storage system that was interfaced with a 180 V DC microgrid using a Split-pi converter. The chosen case study can represent the onboard grid of an unmanned marine vehicle or a scaled prototype of a residential DC microgrid with a 120 V, 60 Hz, single-phase, grid-connected inverter, whose DC link voltage must be higher than 170 V DC. The rated values of the system under study are shown in Table 3.

As for the chosen droop characteristic of the storage converter, in scenario #1 (SS-GN) it was defined by E_{ds} = 180 V and R_{ds} = 0, whereas in scenarios #2 (SD-GN) and #3 (SD-GD), it was expressed by E_{ds} = 180 V and R_{ds} = 2.2 Ω, i.e., imposing a 5% voltage reduction at the nominal current. For the equivalent droop-controlled microgrid generator, the same parameters as those of the storage converter were chosen in scenario #4 (SC-GD). On the other hand, in scenario #3 (SD-GD), the following parameters were used for the droop-controlled microgrid generator: E_d = 198 V and R_d = 9 Ω; with this choice, the storage system did not supply any power for half the rated load of the microgrid, as desired.

Finally, a constant voltage generator E_d = 180 V was considered in scenario #5 (SC-GS) to model the microgrid's stiff voltage generator.

Table 3. Rated values of the system.

Parameter	Symbol	Value
Switching frequency	F_{sw}	20 kHz
Nominal output voltage	V_{2n}	180 V
Nominal input voltage	V_{1n}	50 V
Nominal power	P_n	750 W
Nominal load resistance	R_n	43.2 Ω
Nominal input current	I_{1n}	15 A
Max. charge/discharge current	I_{cx}, I_{dx}	18 A
Nominal output current	I_{2n}	4.167 A
Nominal duty cycle	$\bar{d}$	0.722

The Split-pi's reactive components were sized using (1), (2), (3), and the following parameters were set: $r_{i\%} = \pm 6.0\%$, $r_{ve\%} = \pm 0.2\%$, $r_{v\%} = \pm 0.2\%$. Consequently, the following minimum inductor and capacitor ratings were obtained: L_{min} = 803 µH, $C_{e,min}$ = 113 µF, C_{min} = 419 µF. Aiming to build a converter prototype and due to component availability, slightly higher values were chosen for the reactive components; they are reported in Table 4, together with their parasitic resistances.

Table 4. Reactive components of the Split-pi.

Parameter	Symbol	Value
Inductance value of L	L	1000 µH
Parasitic resistance of L	R_L	65 mΩ
Capacitance value of C_e	C_e	200 µF
Parasitic resistance of C_e	R_e	260 mΩ
Capacitance value of C	C	540 µF
Parasitic resistance of C	R_c	125 mΩ

6. Control System Design

The control system of the Split-pi converter must be designed by considering the specific microgrid scenario in which it will be used. However, in any case, it must be assumed that the converter supplies its rated power without any contribution from the external current or voltage generators, which are seen as disturbances. If the imposed stability margins are sufficiently wide, the designed controllers will be effective also at lighter loads, i.e., with higher values of R. Thus, models A and B must be linearized around the operating point corresponding to the rated values of the duty cycle and state variables: $\bar{d}$ = 0.722 and $\bar{x} = [I_{L10}, I_{L20}, V_{c0}, V_{e0}]' = [15, 4.167, 180, 180]'$. No other condition is needed for model B in scenario #5 (SC-GS). As for model A, instead, it is $R = R_n$ in scenarios #1 (SS-GN) and #2 (SD-GN) and $R = R_n//R_d$ in scenarios #3 (SD-GD) and #4 (SC-GD).

All the above values must be substituted into (A1)–(A6), given in Appendix A, to obtain the coefficients of the transfer functions of interest. Then, designing of the controllers G_{ci1}, G_{cv2}, and G_{ci2} can be performed with classic techniques that involve imposing suitable values of the crossover frequency ω_c and phase margin m_φ and ensuring a suitable gain margin m_g [23]. For each control loop and scenario, the imposed values and the obtained PI coefficients and gain margins are summarized in Tables 5 and 6. Furthermore, a baseline scenario employing the control scheme of Figure 3 with R_d = 0 and without the FF action was also considered for comparison purposes to show the usefulness of such an action.

Table 5. Coefficients of PI regulators in the case of model A.

Loop	Scenario	Value of R	Controller	Imposed ω_c and m_φ	PI Coefficients	Obtained m_g
Current I_{L1}	Baseline #1 (SS-GN) #2 (SD-GN)	R_n	G_{ci_1}	$\omega_c = 3000$ rad/s and $m_\varphi = 85°$	$K_{pi} = 0.0160$ $K_{ii} = 5.3703$	∞
Current I_{L1}	#3 (SD-GD) #4 (SC-GD)	$R_n // R_d$	G_{ci_1}	$\omega_c = 3000$ rad/s and $m_\varphi = 85°$	$K_{pi} = 0.0161$ $K_{ii} = 5.2481$	∞
Voltage V_2 without FF	Baseline	R_n	G_{cv_2}	$\omega_c = 100$ rad/s and $m_\varphi = 85°$	$K_{pv} = 0.2659$ $K_{iv} = 18.6209$	12.7 dB
Voltage V_2 with FF	#1 (SS-GN) #2 (SD-GN)	R_n	G_{cv_2}	$\omega_c = 100$ rad/s and $m_\varphi = 85°$	$K_{pv} = 0.2712$ $K_{iv} = 10.4112$	13.1 dB
Voltage V_2 with FF	#3 (SD-GD)	$R_n // R_d$	G_{cv_2}	$\omega_c = 100$ rad/s and $m_\varphi = 85°$	$K_{pv} = 0.3284$ $K_{iv} = 14.6218$	24.2 dB
Current I_2	#4 (SC-GD)	$R_n // R_d$	G_{ci_2}	$\omega_c = 100$ rad/s and $m_\varphi = 85°$	$K_{pi2} = 0.3746$ $K_{ii2} = 389.045$	23.7 dB

Table 6. Coefficients of PI regulators in the case of model B.

Loop	Scenario	Controller	Imposed ω_c and m_φ	PI Coefficients	Obtained m_g
Current I_{L1}	#5 (SC-GS)	G_{ci_1}	$\omega_c = 3000$ rad/s and $m_\varphi = 85°$	$K_{pi} = 0.0161$ $K_{ii} = 5.0699$	∞
Current I_2	#5 (SC-GS)	G_{ci_2}	$\omega_c = 100$ rad/s and $m_\varphi = 85°$	$K_{pi2} = 1.1953$ $K_{ii2} = 362.22$	13.6 dB with $G_{add}(s)$

It is worth noting that the design of the controllers must be very conservative. By design, the currents I_{L1} and I_{L2} have a significant switching ripple compared to the input/output currents and voltages. Thus, the desired crossover frequency for the I_{L1} loop must be suitably lower than F_{sw} to avoid the switching ripple being processed by the controller. The crossover frequency of the loop for V_2 or I_2 must be even lower for proper decoupling with respect to the inner loop. When the converter supplies a passive load (R_{load}), some ringing can be tolerated, and the usually adopted phase margin (50–60°) is satisfactory. Instead, in the case of an active microgrid, the combined variations of I and R_{load} could determine a significant excursion from the nominal operating point and pronounced under/overshoots; thus, a higher phase margin (i.e., $m_\varphi > 80°$) is required to ensure stability under all the operating conditions. As for the gain margin, the usually adopted criterion (i.e., $m_g > 12$ dB) is enough to ensure robustness against parameter variations.

As for the chosen case study, some noteworthy remarks can be made:

- Regardless of the value of R, models A and B exhibited nearly the same dynamics for I_{L1}; therefore, the corresponding PI regulators G_{ci1} had similar coefficients. On the other hand, the dynamics of I_2 were quite dissimilar and required different G_{ci2} controllers.
- In the case of model B, it could be possible to achieve the desired ω_c and m_φ with a PI or I regulator alone, but the gain margin would be around 6.6 dB due to a resonance peak; thus, the second-order transfer function (26) must be included after the PI regulator to attenuate such a peak and achieve a gain margin of 13.6 dB.
- The dynamics of I_2 were very sensitive to the value of R in model A; thus, an unstable system was obtained in scenario #4 (SC-GD) if the controllers were designed assuming $R = R_n$ instead of $R = R_n // R_d$.
- Without the FF action, the dynamics of V_2 were sensitive to the value of R: a significantly slower behavior was obtained if the controllers were designed assuming $R = R_n$ in scenario #3 (SD-GD) instead of $R = R_n // R_d$; on the other hand, a significant ringing was obtained if the controllers were designed considering $R = R_n // R_d$ in scenarios #1 (SS-GN) and #2 (SD-GN) instead of $R = R_n$.

- Using the FF action, the dynamics of V_2 were pretty insensitive to the value of R; thus, almost no variation was obtained in scenarios #1 (SS-GN), #2 (SD-GN), and #3 (SD-GD) if the controllers were designed when considering either $R = R_n//R_d$ or $R = R_n$.

Several simulations were performed to assess the performance of the controlled system in all the scenarios. Then, a prototype of the Split-pi converter was built, and experimental tests were performed in several conditions that covered the baseline scenario and all the other five scenarios, obtaining successful results. The simulation and experimental results validating the study are presented in part II of this work.

$$G_{add}(s) = \frac{1}{\left(1 + \frac{s}{533}\right)\left(1 + \frac{s}{606}\right)} \tag{26}$$

7. Conclusions

The Split-pi converter is a suitable choice to interface electrical storage systems with DC microgrids. It offers distinct advantages, such as high efficiency, reduced switch count and switching noise, and suitability for multiphase systems at the cost of non-isolated operation. However, to obtain high performance, its control system must be suitably designed according to the specific microgrid scenario in which it will be used.

In this study, five typical microgrid scenarios were identified and analyzed, where each of which required a specific state-space model and a suitable control scheme for the converter. Two different state-space models were presented for the Split-pi converter operating with the storage-side voltage being lower than the grid-side voltage. Both models considered the parasitic elements of the reactive components. As for the control scheme, the number of required control loops depended on the scenario. It was shown that feed-forward action is needed to obtain a high performance in the case of voltage control and that, sometimes, conventional PI regulators alone were not sufficient for stable current control. The most relevant transfer functions of the Split-pi converter were given, together with criteria to design the controllers. Several simulations, as well as experimental tests on a prototype realized in the lab, were performed to validate the study, whose results will be presented in part II of this work.

The approach followed in this study has general validity and can also be followed to devise the state-space model of a Split-pi operating with a storage-side voltage that is higher than the grid-side voltage or when other bidirectional DC/DC converter topologies are employed to interface an ESS with a DC microgrid. Furthermore, the presented study builds the premises for designing unconventional control systems for the Split-pi that are suitable for operating in more than one microgrid scenario.

Institutional Review Board Statement: Not applicable.

Informed Consent Statement: Not applicable.

Data Availability Statement: Not applicable.

Nomenclature

d	Duty cycle
$\bar{d}$	Average duty cycle for state-space model linearization
d_i	Coefficients of the denominator of the transfer function $G_{p1}(s)$
m_φ	Phase margin
m_g	Gain margin
n_i	Coefficients of the numerator of the transfer function $G_{p1}(s)$ and the denominator of $G_{p2}(s)$
$r_{i\%}$	Current ripple in input/output inductor L
$r_{v\%}$	Voltage ripple in the bulk capacitor C
$r_{ve\%}$	Voltage ripple in the external capacitor C_e
u	Input vector of the state-space model of the Split-pi converter
x	State vector of the state-space model of the Split-pi converter
$\bar{x}$	Average state vector for state-space model linearization
y	Output vector of the state-space model of the Split-pi converter
ω_c	Crossover frequency
A,B,C,D	Matrices of the state-space model of the Split-pi converter
C	Bulk capacitor of the Split-pi converter
C_e	External input/output capacitor of the Split-pi converter
$C_{e,min}$	Minimum capacitance value to obtain the chosen ripple $r_{ve\%}$
C_{min}	Minimum capacitance value to obtain the chosen ripple $r_{v\%}$
E_d	Equivalent no-load voltage of the aggregated droop-controlled generators of the microgrid in scenario #5 after load transformation
E_{ds}	No-load voltage used to control the storage converter in droop mode
F_{sw}	Switching frequency
$G_{add}(s)$	Additional transfer function to be included after the PI regulator of current loop for I_2 in the case of stiff microgrid
$G_{ci1}(s)$	Transfer function of the controller for the internal current loop for I_{L1}
$G_{ci2}(s)$	Transfer function of the controller for the external current loop for I_2
$G_{cv2}(s)$	Transfer function of the controller for the voltage loop for V_2
$G_{p1}(s)$	Transfer function of the process that expresses the relationship between d and I_{L1}
$G_{p2}(s)$	Transfer function of the process that expresses the relationship between I_{L1} and I_2
I	Current supplied by the aggregated current generators of the microgrid managed by the EMS
I_1	Input current of the Split-pi converter (port 1, storage-side)
I_{1n}	Nominal input current (storage-side)
I_2	Output current of the Split-pi converter (port 2, grid-side)
I_{2n}	Nominal output current (grid-side)
I_{2ref}	Reference current computed using the EMS for the storage converter controlled in current mode
I_d	Current supplied by the aggregated droop-controlled generators of the microgrid
I_{cx}	Maximum charging current of the storage system
I_{dx}	Maximum discharging current of the storage system
I_{eq}	Equivalent current generator considered as active load in scenarios #1–#4 after load transformation
I_{L1}	Current of the leftmost inductor of the Split-pi converter (port 1, storage-side)
I_{L10}	Average current value of the leftmost inductor for model linearization
I_{L2}	Current of the rightmost inductor of the Split-pi converter (port 2, grid-side)
I_{L20}	Average current value of the rightmost inductor for model linearization
K_{ii}	Integral gain of the PI regulator of current loop for I_{L1}
K_{ii2}	Integral gain of the PI regulator of current loop for I_2
K_{iv}	Integral gain of the PI regulator of voltage loop for V_2
K_{pi}	Proportional gain of the PI regulator of current loop for I_{L1}

K_{pi2} Proportional gain of the PI regulator of current loop for I_2

K_{pv} Proportional gain of the PI regulator of voltage loop for V_2

L Inductor at input/output ports of the Split-pi converter

L_{min} Minimum inductance value to obtain the chosen ripple $r_{i\%}$

P_n Nominal power of the storage converter

R Equivalent load resistance considered in scenarios #1–#4 after load transformation

R_c Parasitic resistance of bulk capacitor of the Split-pi converter

R_d Equivalent droop resistance of the aggregated droop-controlled generators of the microgrid

R_{ds} Droop resistance used to control the storage converter in droop mode

R_e Parasitic resistance of external input/output capacitor of the Split-pi converter

R_L Parasitic resistance of inductor at input/output ports of the Split-pi converter

R_{load} Equivalent load resistance of the microgrid

R_k Fictitious resistance term appearing in the transfer function $G_{p2}(s)$

R_n Nominal load resistance

SOC State of charge of the storage system

V_1 Input voltage of the Split-pi converter (port 1, storage-side)

V_{1n} Nominal input voltage (storage-side)

V_2 Output voltage of the Split-pi converter (port 2, grid-side)

V_{2n} Nominal output voltage (grid-side)

V_{2ref} Reference output (microgrid) voltage for the storage converter controlled in droop mode

V_c Voltage of the bulk capacitor of the Split-pi converter

V_{c0} Average voltage value of the bulk capacitor for model linearization

V_e Voltage of the external input/output capacitor of the Split-pi converter

V_{e0} Average voltage value of the external capacitors for model linearization

Appendix A. Coefficients of the Transfer Functions of Model A

The coefficients of the transfer functions (14) and (15) of state-space model A are expressed using the following equations:

$$
\begin{cases}
n_3 = \dfrac{V_{c0} + R_c(I_{L10} - I_{L20})}{L} \\[2mm]
n_2 = \dfrac{(1-\bar{d})I_{L10}(L - CR_c^2) + n_3 LC\left(R_p + R_L + R_c + \frac{L}{C_e R_{sum}}\right)}{L^2 C} \\[2mm]
n_1 = \dfrac{(1-\bar{d})I_{L10}\left(R_p + R_L - R_c + R_c\frac{\frac{L}{R_c} - R_c C}{C_e R_{sum}}\right) + n_3 L\left(\frac{CR^2}{C_e R_{sum}^2} + \frac{CR_{tot}}{C_e R_{sum}} + 1\right)}{L^2 C} \\[2mm]
n_0 = \dfrac{(1-\bar{d})I_{L10}(R + R_L - R_c) + n_3 L}{L^2 C} \cdot \dfrac{1}{C_e R_{sum}}
\end{cases}
\tag{A1}
$$

$$
\begin{cases}
d_4 = 1 \\[2mm]
d_3 = \dfrac{R_p + 2R_L + (2-\bar{d})R_c}{L} + \dfrac{1}{C_e R_{sum}} \\[2mm]
d_2 = \dfrac{R + 2R_L + (2-\bar{d})R_c}{L} \cdot \dfrac{1}{C_e R_{sum}} + \\[2mm]
\quad \dfrac{R_L^2 + R_L R_p + R_c\left((2-\bar{d})R_L + \bar{d}(1-\bar{d})R_c + (1-\bar{d})R_p\right)}{L^2} + \dfrac{1 + (1-\bar{d})^2}{LC} \\[2mm]
d_1 = \dfrac{(2-\bar{d})R_L + \bar{d}(1-\bar{d})(R_c - R_L - R_p) + (1-\bar{d})R_p}{L^2 C} + \\[2mm]
\quad \left(\dfrac{R_L^2 + R_L R + R_c\left((2-\bar{d})R_L + \bar{d}(1-\bar{d})R_c + (1-\bar{d})R\right)}{L^2} + \dfrac{1 + (1-\bar{d})^2}{LC}\right) \cdot \dfrac{1}{C_e R_{sum}} \\[2mm]
d_0 = \dfrac{(2-\bar{d})R_L + \bar{d}(1-\bar{d})(R_c - R_L - R) + (1-\bar{d})R}{L^2 C} \cdot \dfrac{1}{C_e R_{sum}}
\end{cases}
\tag{A2}
$$

$$
R_k = \dfrac{\left(1-\bar{d}\right)(V_{c0} - I_{L20}R_c)}{I_{L10}} - R_L
\tag{A3}
$$

Appendix B. Coefficients of the Transfer Functions of Model B

The coefficients of the transfer functions (24) and (25) of state-space model B are expressed using the following equations:

$$
\begin{cases}
n_2 = \dfrac{V_{c0} + R_c(I_{L10} - I_{L20})}{L} \\[2mm]
n_1 = \dfrac{(1 - \bar{d})I_{L10}(L - CR_c^2) + n_2 LC(R_L + R_c)}{L^2 C} \\[2mm]
n_0 = \dfrac{(1 - \bar{d})I_{L10}(R_L - R_c) + n_2 L}{L^2 C}
\end{cases}
\tag{A4}
$$

$$
\begin{cases}
d_3 = 1 \\[2mm]
d_2 = \dfrac{2R_L + (2 - \bar{d})R_c}{L} \\[2mm]
d_1 = \dfrac{R_L^2 + R_c\big((2 - \bar{d})R_L + \bar{d}(1 - \bar{d})R_c\big)}{L^2} + \dfrac{1 + (1-\bar{d})^2}{LC} \\[2mm]
d_0 = \dfrac{(2 - \bar{d})R_L + \bar{d}(1 - \bar{d})(R_c - R_L)}{L^2 C}
\end{cases}
\tag{A5}
$$

$$
R_k = \frac{(1 - \bar{d})(V_{c0} - I_{L20}R_c)}{I_{L10}} - R_L
\tag{A6}
$$

References

1. Di Piazza, M.C.; Luna, M.; Pucci, M.; La Tona, G.; Accetta, A. Electrical Storage Integration into a DC Nanogrid Testbed for Smart Home Applications. In Proceedings of the 2018 IEEE International Conference on Environment and Electrical Engineering and 2018 IEEE Industrial and Commercial Power Systems Europe (EEEIC / I&CPS Europe), Palermo, Italy, 12–15 June 2018; pp. 1–5.
2. Chub, A.; Vinnikov, D.; Kosenko, R.; Liivik, E.; Galkin, I. Bidirectional DC–DC Converter for Modular Residential Battery Energy Storage Systems. *IEEE Trans. Ind. Electron.* **2020**, *67*, 1944–1955. [CrossRef]
3. Sim, J.; Lee, J.; Choi, H.; Jung, J.H. High Power Density Bidirectional Three-Port DC-DC Converter for Battery Applications in DC Microgrids. In Proceedings of the 2019 10th International Conference on Power Electronics and ECCE Asia (ICPE 2019—ECCE Asia), Busan, Korea, 27–30 May 2019; Volume 3, pp. 843–848.
4. Byrne, R.H.; Nguyen, T.A.; Copp, D.A.; Chalamala, B.R.; Gyuk, I. Energy Management and Optimization Methods for Grid Energy Storage Systems. *IEEE Access* **2018**, *6*, 13231–13260. [CrossRef]
5. La Tona, G.; Luna, M.; Di Piazza, A.; Di Piazza, M.C. Towards the real-world deployment of a smart home EMS: A DP implementation on the Raspberry Pi. *Appl. Sci.* **2019**, *9*, 2120. [CrossRef]
6. Accetta, A.; Pucci, M. Energy Management System in DC Micro-Grids of Smart Ships: Main Gen-Set Fuel Consumption Minimization and Fault Compensation. *IEEE Trans. Ind. Appl.* **2019**, *55*, 3097–3113. [CrossRef]
7. Gorji, S.A.; Sahebi, H.G.; Ektesabi, M.; Rad, A.B. Topologies and Control Schemes of Bidirectional DC–DC Power Converters: An Overview. *IEEE Access* **2019**, *7*, 117997–118019. [CrossRef]
8. Beheshtaein, S.; Cuzner, R.M.; Forouzesh, M.; Savaghebi, M.; Guerrero, J.M. DC Microgrid Protection: A Comprehensive Review. *IEEE J. Emerg. Sel. Top. Power Electron.* **2019**, *6777*. [CrossRef]
9. Han, S.; Divan, D. Bi-directional DC/DC converters for plug-in hybrid electric vehicle (PHEV) applications. In Proceedings of the 2008 Twenty-Third Annual IEEE Applied Power Electronics Conference and Exposition, Austin, TX, USA, 24–28 February 2008; pp. 784–789.
10. Tytelmaier, K.; Husev, O.; Veligorskyi, O.; Yershov, R. A review of non-isolated bidirectional dc-dc converters for energy storage systems. In Proceedings of the 2016 II International Young Scientists Forum on Applied Physics and Engineering (YSF), Kharkiv, Ukraine, 10–14 October 2016; pp. 22–28.
11. Odo, P. A Comparative Study of Single-phase Non-isolated Bidirectional dc-dc Converters Suitability for Energy Storage Application in a dc Microgrid. In Proceedings of the 2020 IEEE 11th International Symposium on Power Electronics for Distributed Generation Systems (PEDG), Dubrovnik, Croatia, 28 September–1 October 2020; pp. 391–396.
12. Crocker, T.R. Power Converter and Method for Power Conversion. U.S. Patent No. 20040212357A1, 28 October 2004.
13. Khan, S.A.; Pilli, N.K.; Singh, S.K. Hybrid Split Pi converter. In Proceedings of the 2016 IEEE International Conference on Power Electronics, Drives and Energy Systems (PEDES), Trivandrum, India, 14–17 December 2016; pp. 1–6.
14. Sobhan, S.; Bashar, K.L. A novel Split-Pi converter with high step-up ratio. In Proceedings of the 2017 IEEE Region 10 Humanitarian Technology Conference (R10-HTC), Dhaka, Bangladesh, 21–23 December 2017; pp. 255–258.
15. Ahmad, T.; Sobhan, S. Performance analysis of bidirectional split-Pi converter integrated with passive ripple cancelling circuit. In Proceedings of the 2017 International Conference on Electrical, Computer and Communication Engineering (ECCE), Cox's Bazar, Bangladesh, 16–18 February 2017; pp. 433–437.
16. Singhai, M.; Pilli, N.K.; Singh, S.K. Modeling and analysis of split-Pi converter using State space averaging technique. In Proceedings of the 2014 IEEE International Conference on Power Electronics, Drives and Energy Systems (PEDES), Mumbai, India, 16–19 December 2014; pp. 1–6.

17. Maclaurin, A.; Okou, R.; Barendse, P.; Khan, M.A.; Pillay, P. Control of a flywheel energy storage system for rural applications using a Split-Pi DC-DC converter. In Proceedings of the 2011 IEEE International Electric Machines & Drives Conference (IEMDC), Niagara Falls, ON, Canada, 15–18 May 2011; pp. 265–270.

18. Sabatta, D.; Meyer, J. Super capacitor management using a Split-Pi symmetrical bi-directional DC-DC power converter with feed-forward gain control. In Proceedings of the 2018 International Conference on the Domestic Use of Energy (DUE), Cape Town, South Africa, 3–5 April 2018; pp. 1–5.

19. Monteiro, V.; Oliveira, C.; Rodrigues, A.; Sousa, T.J.C.; Pedrosa, D.; Machado, L.; Afonso, J.L. A Novel Topology of Multilevel Bidirectional and Symmetrical Split-Pi Converter. In Proceedings of the 2020 IEEE 14th International Conference on Compatibility, Power Electronics and Power Engineering (CPE-POWERENG), Setubal, Portugal, 8–10 July 2020; pp. 511–516.

20. Alzahrani, A.; Shamsi, P.; Ferdowsi, M. Single and interleaved split-pi DC-DC converter. In Proceedings of the 2017 IEEE 6th International Conference on Renewable Energy Research and Applications (ICRERA), San Diego, CA, USA, 5–8 November 2017; pp. 995–1000.

21. Mohan, N.; Undeland, T.M.; Robbins, W.P. *Power Electronics. Converters, Applications and Design*, 3rd ed.; John Wiley and Sons, Inc.: Hoboken, NJ, USA, 2003.

22. Middlebrook, R.D.; Cuk, S. A general unified approach to modelling switching-converter power stages. In Proceedings of the 1976 IEEE Power Electronics Specialists Conference, Cleveland, OH, USA, 8–10 June 1976; pp. 18–34.

23. Fung, H.-W.; Wang, Q.-G.; Lee, T.-H. PI Tuning in Terms of Gain and Phase Margins. *Automatica* **1998**, *34*, 1145–1149. [CrossRef]